Title

Applying Pattern Recognition to High-Resolution Images to Determine Cellular Signaling Status

Journal

IEEE Transactions on NanoBioscience, 16(6)

ISSN

1536-1241

Authors

Lohrer, Michael F
Hanna, Darrin M
Liu, Yang
et al.

Publication Date

2017-09-01

DOI

10.1109/tnb.2017.2717871

Peer reviewed

HHS Public Access

Author manuscript

IEEE Trans Nanobioscience. Author manuscript; available in PMC 2018 September 01.

Published in final edited form as:

IEEE Trans Nanobioscience. 2017 September ; 16(6): 438–446. doi:10.1109/TNB.2017.2717871.

Applying Pattern Recognition to High-Resolution Images to Determine Cellular Signaling Status

Michael F. Lohrer,
Department of Electrical and Computer Engineering, Oakland University, Rochester MI 48309, USA

Darrin M. Hanna* **[Member, IEEE]**,
Department of Electrical and Computer Engineering, Oakland University, Rochester MI 48309, USA

Yang Liu,
Department of chemistry, University of California, Davis, CA 95616 USA

Kang-Hsin Wang,
Department of chemistry, University of California, Davis, CA 95616 USA

Fu-Tong Liu,
Department of Dermatology, University of California, Davis Medical Center, Sacramento, CA 95817, USA

Ted A. Laurence, and
Lawrence Livermore National Laboratory, Livermore, CA 94550, USA

Gang-Yu Liu*
Department of chemistry, University of California, Davis, CA 95616 USA

Abstract

Two frequently used tools to acquire high-resolution images of cells are scanning electron microscopy (SEM) and atomic force microscopy (AFM). The former provides a nanometer resolution view of cellular features rapidly and with high throughput, while the latter enables visualizing hydrated and living cells. In current practice, these images are viewed by eye to determine cellular status, e.g. activated versus resting. Automatic and quantitative data analysis is lacking. This work develops an algorithm of pattern recognition that works very effectively for AFM and SEM images. Using rat basophilic leukemia (RBL) cells, our approach creates a support vector machine (SVM) to automatically classify resting and activated cells. 10-fold cross-validation with cells that are known to be activated or resting gives a good estimate of the generalized classification results. The pattern recognition of AFM images achieves 100% accuracy, while SEM reaches 95.4% for our images as well as images published in prior literature. This outcome suggests that our methodology could become an important and frequently used tool for researchers utilizing AFM and SEM for structural characterization as well as determining cellular signaling status and function.

*Authors to whom correspondence should be addressed, dmhanna@oakland.edu, gyliu@ucdavis.edu.

I. Introduction

Cellular shape, morphology, and intracellular membrane features are frequently used as direct readouts of the biological status of the cell, such as activation, spreading, motility, malignancy and death [1–10]. Well-known examples include donut-shaped versus sickle-shaped red blood cells indicating a healthy and ill status [11, 12], dendritic versus relatively smooth morphology are associated with mature and immature dendritic cells (DCs) [13–16]. Modern bioimaging technology enables visualization of cells with much higher spatial resolution than conventional optical microscopy. Scanning electron microscopy (SEM) allows the shape as well as detailed cellular features such as filopodia, lamellar podia, podosome, and microvilli to be visualized [17–22]. While simple and rapid, SEM requires cells to be dry and stained with heavy metal ions to enhance contrast [17–22]. Atomic force microscopy (AFM), although relatively low in throughput, enables visualizing cellular morphology and structural features for hydrated and even living cells in near-physiological conditions [23–31]. Researchers have just begun to explore the qualitative and quantitative information from these high resolution structural features in correlation with the biological status function of cells, such as the degree of motility and malignancy [32–37].

Using a specific cell type as an example, rat basophilic leukemia (RBL) cells, prior investigations by us and other researchers have studied the cellular activation processes, in the investigations of allergy [4, 15, 29, 30, 38–47]. These investigations revealed that these nanometer- to micrometer-scale structural features are directly related to cellular signaling processes [4, 15, 29, 38–45]. In the resting state, the RBL membrane is relatively smooth as characterized by the presence of microvilli, shown in Fig. 1a and Fig. 1c. Upon IgE antibody-mediated activation, also known as immediate-type hypersensitivity response or allergy, folded features such as ridges are observed on cell membranes, illustrated in Fig. 1b and Fig. 1d [28–30, 43, 47–49].

At present, these high-resolution images are viewed by eye as a qualitative readout for the activation status of the RBL cells [20, 26, 28, 43, 47]. Systematic, automatic, and quantitative data analysis is severely limited [45, 50, 51]. The challenges include the complexity of cellular systems, the relatively small number of high resolution images in comparison to material imaging, and the detailed communication and collaboration required among scientists in imaging, cellular bioscience, and pattern recognition. Our past work has demonstrated the importance and effectiveness of utilizing machine learning for experimental data analysis [52–54]. This work reports our approach which introduces pattern recognition as part of a data analysis of these high-resolution images of RBL cells, and uses the outcome to classify each cell based on activation status. Among various tools and approaches utilized in pattern recognition, we have identified and developed approaches that best address the challenges of this work. More detailed discussion of experimental design and validation can be found in supplementary materials. For this work, 35 AFM images were acquired from 8 independent sets of experiments. Among them 10 RBL cells were in a resting state, and 25 were activated via antibody mediated processes. In addition, 99 SEM images were taken from 13 sets of experiments. Among them, 43 RBL cells were resting, and 56 were activated. The optimization and simplification are performed to enhance speed and efficiency of our pattern recognition algorithms. The results exhibit very high

accuracy in determining the activation status of RBLs. We anticipate this approach shall have generic applications to a wide range of cell types and signaling processes. Further development shall harness important biological insights from the high-resolution images that modern technologies enable.

II. Image Preprocessing

AFM and SEM images of RBL cells are typically acquired by optimizing experimental conditions to reveal cellular features that are of interest to individual researchers. The technical specifications and user skills vary from one laboratory to another. As such, the image size, signal-to-noise ratio, background, and contrast often vary and are highly nonuniform and non-standard from image to image and from one laboratory to another. Therefore, preprocessing is necessary to assure that structural features pertaining to cellular signaling processes are revealed accurately before applying pattern recognition. In this work, each cell undergoes a process of background subtraction, noise reduction, and finally circular cropping to a standard 512×512 pixel resolution, as summarized in Fig. 2. These steps assure localizing the cells while normalizing the size. These standardized circular images are ready for the subsequent steps in pattern recognition (see Section III).

The image processing steps are identical regardless of the nature of images, e.g. AFM or SEM. Fig. 2 reveals the key steps and corresponding results for images acquired using AFM (left) and SEM (right), respectively, to illustrate and compare. The first step in preprocessing is to enhance intrinsic cellular features in the images by eliminating the background present in images. Since the background is highly local, we adopted a white top-hat transform (WTHT) [55]. The WTHT is designed to extract each feature (peak in imaging contrast) in an image by subtracting the background surrounding it. The WTHT is defined as the difference between the input image and its opening using

$$T_W(I) = I - I \circ S \quad (1)$$

where I is the input image, $T_W(I)$ is the white top-hat transform, S is a structuring element and ◦ is the opening operator. An opening with a 10×10 circular structuring element was used. The gray-scale opening serves to filter out the cellular features, leaving only the general background patterns. The image formed after the opening was then subtracted from the original so that only the features remain.

After performing the WTHT, the result was normalized so that the darkest pixel is 0 and the brightest is 1. A 7×7 median filter was then applied to remove any noise and only allow true features. Next, an adaptive threshold was applied to convert the grayscale image to black and white. The adaptive threshold finds the appropriate threshold for each region of an image. The image was severely blurred with a 25×25 average filter and the difference between the filtered image and the original served to further increase contrast. Finally, a standard gray threshold was applied using Otsu's method [56] to determine the threshold.

For RBLs under this investigation, we added one more step to enable cell selection even in the case of congregation or confluence of cells causing overlap at cellular peripheral regions. Considering the focus of this pattern recognition targets membrane features, we subjected the black-and-white images to circular cropping. A morphological closing operation with a 9×9 disk structuring element was performed to fill in small holes in the resulting black-and-white images. Then the largest connected component of white pixels was taken to be the cell, from which the centroid, (x, y) and radius, R, were calculated. Then, a square mask containing the circle with center (x, y) and radius of 0.9R was applied to original image. Only the pixels within the circle were kept and the rest were set to 0 (black) so that only membrane features were analyzed. The center and radius of the cell are used to crop the original image so that it contains only the cell image. The cropped images were then scaled to a square of 512x512 pixels so that the feature generation step has uniformly-sized input images. The resulting image representing the initial cellular data was utilized for the next step of feature generation.

III. Feature Generation

The goal of the feature generation step is to create a set of data that can be used by the classifier to distinguish activated from resting cells. Since the cell's biological status is correlated with overall cellular shape, geometry, size as well as membrane features [28–30, 38, 47–49], our feature generation and selection must reflect upon these structural characteristics. Two feature generation methods that we decided to employ for recognizing nanoscopic features of RBL cells are Local Binary Patterns (LBP) and Histogram of Oriented Gradients (HOG). LBP [57] was designed to describe textures in an image. Since the difference between activated and resting RBL cells lies primarily in the membrane features, density, and size of villi and ridges, texture differences are a dominant feature. HOG [58] has been proven to be effective for recognizing object shape and geometry; for example, it is often used for differentiating humans from other objects in images [58–60]. In order to determine activation status of mast cells and, at the same time create a more general system capable of accessing other cell signaling processes for a wide range of different cell types, combined LBP and HOG features are necessary to achieve accurately classification.

A. Local Binary Patterns

We applied LBP by calculating a binary code for each pixel location from the grayscale image. The code was created by comparing the center pixel in a 3×3 area and its neighbors, as shown in Fig. 3. If the center pixel was greater in value than its neighbor, the number 0 was written in its place, otherwise the pixel has the value of 1. Starting with the top-left value and moving clockwise, the 8-bit binary value was created from the 0's and 1's. Therefore, for each pixel in the image, a new number between 0 and 255 in decimal is generated. This process is illustrated in Fig. 3.

The image was then divided into 256 windows of size 32x32. In each window a histogram was created of the 1024 binary codes encountered. A window size of 32x32 was chosen to match the scale appropriate with the ridge features in the cell images, the vast majority of ridges occupied less than one-third of a 32x32 window.

Using the original LBP method, there would be 256 bins in each histogram. In our algorithm however, uniform binary patterns were used. An 8-bit binary pattern is uniform if it has at most two 0-1 or 1-0 transitions. The example given in Fig. 3 is non-uniform because it has four transitions. The histogram is made by creating a bin for each uniform pattern and placing the sum of all non-uniform patterns in a single bin. There are 58 uniform patterns, so there are 59 total bins.

Each histogram is then normalized using the L^2 (Euclidean) norm, so that the new histogram values are given by

$$\boldsymbol{h_n} = \frac{\boldsymbol{h}}{\|\boldsymbol{h}\|_2} = \frac{h}{\sqrt{h_1^2 + \ldots + h_n^2}} \quad (2)$$

where $\boldsymbol{h}$ is the histogram vector and $\boldsymbol{h_n}$ is the normalized histogram vector. The resulting feature vector is formed by concatenating the normalized histograms. Our 512×512 images were divided into 32×32 windows, resulting in $16^2 = 256$ histograms. Since each histogram has 59 bins the feature vector was 15,104 elements long.

B. Histogram of Oriented Gradients

We found that adding HOG feature descriptors to LBP more completely represented cell status. The HOG starts by computing the gradient of the image, given by

$$\nabla f \equiv \begin{bmatrix} G_x \\ G_y \end{bmatrix} = \begin{bmatrix} \frac{\partial f}{\partial x} \\ \frac{\partial f}{\partial y} \end{bmatrix} \quad (3)$$

where $\partial f / \partial x$ is the gradient in the x-direction and $\partial f / \partial y$ is the gradient in the y-direction [61]. Thus from the input image, two output images are generated: the G_x and G_y gradient images. By taking

$$\frac{\partial f}{\partial x} = f(x+1) - f(x-1) \quad (4)$$

for $\partial f / \partial x$ and similarly for $\partial f / \partial y$, we can produce the symmetric 1-dimensional filter [−1 0 1] and its transpose $[-1\ 0\ 1]^T$. Thus we compute G_x by

$$G_x = [-1\ \ 0\ \ 1] * \boldsymbol{I} \quad (5)$$

and G_y by

$$G_y=[-1\ 0\ 1]^T * \boldsymbol{I} \quad (6)$$

where I is the input image and * is the convolution operator. Rather than the gradient in the x- and y-direction, the HOG method utilizes the magnitude and direction of the gradient given by

$$G=\sqrt{G_x^2+G_y^2} \quad (7)$$

$$\theta=\tan^{-1}\left(\frac{G_y}{G_x}\right). \quad (8)$$

The HOG method used subdivides the image into 8×8 windows. Just as with LBP, HOG creates a histogram over each window. Except with HOG the histogram bins are based on the orientation of the gradient at each pixel and therefore a window size smaller than 32×32, (i.e. one quarter of the size) is desirable to concentrate on more detailed pattern orientation. Here the absolute value of the orientation angles were taken and placed in 9 bins evenly spaced between 0 and 180°. This partitions the oriented gradients into 20-degree increments which is representative of the relatively smooth and few directional changes of the structural features observed in activated cells. The histogram was created by adding the sum of the magnitudes of each gradient that are within a bin's range of angles. For example, the magnitudes of all gradients in a single 8x8 window with angles in the range [0,20) are summed to form a single bin.

The histograms for each window were then normalized. To account for changes in contrast throughout the image, normalization was performed within blocks surrounding each window. The block size used in this method is 2×2, again one quarter of the size of the HOG window, with an overlap of one window width. An example is shown in Fig. 4. The example image is made up of 6 windows W_{ij} for i=1,2 and j=1,2,3. The histograms of each window W_{ij} is $H(W_{ij})$. To create the first block the windows $H(W_{11})$, $H(W_{12})$, $H(W_{21})$, and $H(W_{22})$ are concatenated. Since the overlap is one window wide on each side, block 2 is created by concatenating $H(W_{12})$, $H(W_{13})$, $H(W_{22})$, and $H(W_{23})$. After each block is created it is normalized in the same way the LBP histogram vectors are normalized, using equation 2. Concatenating all the normalized blocks gives a feature vector for the entire image that is 142,884 elements long.

IV. Feature Selection and Classification

A. Feature Selection and Cross Validation

Feature generation methods such as LBP and HOG produce very large feature vectors. Using all of these features for classification is neither time efficient nor necessary as not all

features are biologically “equal” in the context of cellular biology and imaging contrast. Many of the feature vectors are redundant, unnecessary, or insignificant. Therefore, extracting meaningful features from the whole set is a necessary and important step for fast, accurate classification. A Welch’s t-test [62] was employed which exploits the use of a null hypotheses to understand the variation among the vast number of features in predicting the known classes. The Welch’s t-test has been used successfully in prior investigations to select features that contribute most to classification, proven particularly effective for applications with a limited number of training data where each class does not necessarily have equal variance among samples [63, 64]. Welch’s t-test assigns a p-value to each feature and it is used to determine how useful the feature is at discriminating between the two classes. A Welch’s t-test was used over a standard t-test due to the features and classes having unequal variances. This type of ranking with p-values can be used to reduce the amount of features used.

Automatic recognition of activation status is accomplished through a classification process. In pattern recognition, a set of features is mapped to a label. Classification is a type of pattern recognition that labels the input set of features with one of several classes. In this case the classes are the two RBL cell states of interest: resting and activated.

Many methods for classifying input feature vectors exist. We chose to use a support vector machine (SVM) since we have a smaller number of data points than features. This method uses hyperplanes to divide the two classes of interest, in this case an activated or resting RBL cell. Each feature point is comprised of a large number of individual feature values provided by the histograms created using LBP and HOG as selected during feature reduction. A linear kernel modeling the hyperplane was used and solved by the sequential minimal optimization algorithm [65]. Ultimately, one hyperplane is chosen which either maximizes the distance between the plane and the feature points of each class, or minimizes the amount of misclassified feature points on either side of the hyperplane, depending on whether or not the data are linearly separable [66].

We also tested the performance with another known pattern recognition protocol, a decision tree approach [67]. Systematic comparison reveals that SVM finds a more optimal partitioning of the feature space than a decision tree and ultimately yielding more accurate assignments of cellular signaling status. On the other hand, the decision tree approach is faster and more effective if training data sets are large. For determining RBL cell activation, a large number of training data are not necessary to achieve accurate results. Therefore SVM is more desirable.

To ensure the validity of the SVM classifier on more than just a single training set of images, 10-fold cross-validation was utilized. Cross-validation has proven valid and effective in situations where the number of images or data is less than massive [66, 68–70]. We note that 35 AFM images of RBL cells may seem to be a limited data set, but this number is among the highest in peer investigations [71–73]. SEM technology is relatively higher throughput, and 99 images were used in this work, with more images available in literature. In the interest of developing a generic algorithm, the same cross-validation was applied to SEM images.

In our cross-validation method, the full set of images available was partitioned into 10 disjoint subsets randomly. In each fold, a single subset of the 10 was kept aside for testing the model and the remaining 9 subsets were used as training data. The SVM classifier was trained on the 9 training subsets and the results of the fold are recorded. This process was repeated until all 10 subsets have been used for testing. The correctly classified and misclassified results of each fold were tallied to produce the accuracy measure of the 10-fold cross-validation.

Due to the random assignment of subsets in the cross-validation, the results can vary slightly between trials. To reduce the variance of the cross-validation results 30 independent trials are performed. In each trial, 10-fold cross-validation is performed with a new randomly-divided set of subsets. The 30 results are averaged to create the final accuracy for the classification method.

B. Classification Using Various Types of Images

SEM images typically consist of a single type of contrast, the intensity of secondary electrons at the detector, while the AFM images are acquired from multiple contrast mechanisms: topography, deflection, and lateral force images. In each contrast type, our algorithm iteratively generates a profile of classification results using the feature selection method described. Fig. 5 shows the results of classification given the top 1 to 40 features selected by the p-values. For each feature number, 30 trials were run to reduce variance of the results. The trend and detailed feature number dependence guide our choice of image type and the minimum feature numbers needed for accurate pattern recognition in our chosen investigations such as AFM or SEM. As shown in Fig. 5, the feature number dependence varies with the origin of the contrast. Topography which measures the physical height of surface structures, yields a high accuracy of 100%, at 10 features. Deflection which measures AFM cantilever bending when scanning over surface structures has similar behavior. Lateral force images result in slower increases and do not reach 100% accuracy until 29 features are used. To determine the number of features for the algorithm, we chose the number of features in which there is less than 1% change in accuracy upon increasing the number of features by one with such stability maintained in 10 consecutive increases. For AFM topography, the transition occurs at 32 features, that is, little changes are seen from 33 – 43. For deflection and lateral force, transitions are 20 and 14 features, respectively. This approach is not limited to these three types and could include others such as elasticity, amplitude, and phase in AFM imaging. Based on the trend and stability, we decided to use AFM topographic images at 40 features. For SEM images, the stability is not reached until the number of features is much higher as shown in Fig. 6, where 95.7% accuracy is reached and stabilized at 135 features. Therefore, at least 135 features are needed in our pattern recognition algorithm in the case of SEM image analysis.

These results are very encouraging as the pattern recognition program has no knowledge nor input to reveal physical origin of image contrast, but seems to yield more accurate results using fewer features from image types with a clear physical base, such as AFM topography. As a comparison, the SEM images were analyzed and shown in Fig. 5, where the accuracy increases slower than AFM, and seems to plateau at 90% accuracy upon using 20 features.

The secondary electron intensity is not as simple as AFM topography because many factors could contribute to the contrast such as topography, OsO_4 distribution, and potential distribution due to material and physical features [17, 74–76]. To test how many features are required for accurate SEM classification results, cross-validation and accuracy measurement was performed for an increasing number of features from 1 to 160 in order of p-value computed by the Welch's t-test. While the Welch's t-test ranks an individual feature's ability to discriminate between classes, the accuracy does not necessarily increase monotonically with increasing numbers of features. It is more meaningful to observe the trend, as shown in Fig. 6. The graph of the accuracy measured for the SEM data is given in Fig. 6 with the AFM topography image accuracy shown for comparison. In these cases, more features, up to 135, seem to provide an effective remedy to ensure accuracy.

V. Results And Discussion

To reveal and evaluate the performance of our method, a set of AFM topography images of RBL cells were first used which contains 10 resting and 25 activated RBL cells for a total of 35 images. Following the image preprocessing and normalization, the 35 images were divided into 10 subsets, the first 5 contains 3 images/subset while the other 5 have 4 images/subset. An SVM classifier is created and its performance is measured, following the protocols discussed previously.

The results of the AFM image classification are shown in Table I. Based on the protocol from the previous section, 40 features were selected and used for recognition. The outcome is reported in a confusion matrix. Confusion matrices reveal the correctly classified results as well as the false positives and negatives. Since the training and testing sets for cross-validation were chosen randomly, 100 independent trials were run. The results shown are the averages of those trials with the standard deviation. The accuracy is calculated by taking the sum of the diagonal of the confusion matrix which represents the number of correct classifications, divided by the total number of cell images. In the case of AFM image classification, all 25 activated cells were classified correctly by our algorithm and all 10 resting cells were correctly identified. Therefore, 100% accuracy is achieved. To compare to SEM results later, we used 135 features, yielding the same accuracy of 100%.

The experiments were repeated using the same method with 99 SEM images. If 40 features were used, the accuracy only reached 90.1%, as shown in Table II. On average 38.9 of the 43 resting cells and 50.3 of the 56 activated cells were correctly classified which gives an overall accuracy of 90.1%. The 95.4% average accuracy can be achieved when increasing the number of features to 135, which yields optimal results with our method using SEM images.

To test the performance of our methodology, we randomly and blindly selected six SEM images that were acquired and published by other teams [47, 77]: three resting RBL cells and three more activated. These images were cropped from the paper's PDF file. Using the images taken directly from the papers, our classifier rapidly and correctly identified the cell status for 5 out of the 6 images using only 135 features. Upon closer examination of the only

false classification, our program indicates a low signal-to-noise ratio associated with that particular image, which was cropped from the publication in pdf format.

To test the robustness and limitations of our approach, we repeated our experiments using 2-fold cross-validation, that is, 50% of the images were used for training and the other 50% were used for testing. As before, the images were split into the training and testing sets at random, 100 times, to reduce variance. For 40 features, the average accuracies of this validation method were 90.9% and 99.5% for SEM and AFM topography, respectively. For 135 features, the average accuracies were 95.1% and 99.5% for SEM and AFM topography, respectively. We infer that our 10-fold cross-validation is sufficient to ensure accuracy in terms of determining cellular activation.

VI. Conclusions

This work represents our initial attempt to provide an accurate and automated system for determining cell signaling status from high resolution images of single cells. Both AFM and SEM images were utilized to test our approach. Procedures included using local binary patterns and histogram of gradients as features, reducing the feature space using t-test analysis, and training a support vector machine. Using this procedure we demonstrated that our system is capable of finding the most useful contrast type for determining cell activation status accurately. More than 95% accuracy was achieved for AFM and SEM images. For situations with characteristic structural features such as membrane ridges captured by AFM, 100% accuracy was attained with only 10 features. Even with mixed contributions to image contrast, such as SEM images, more than 95% accuracy was obtained with 135 features. These initial successes are very encouraging. Work is in progress to investigate more cell types and various signaling processes to further optimize these data analysis algorithms. We selected mast cell activation as a starting point to demonstrate the complexity and effectiveness of applying machine learning and pattern recognition to cellular biochemistry research. Note that mast cell activation is a relatively simple problem in comparison to the complexity of cellular images. We fully anticipate that more pattern recognition tools and protocols will have to be added and developed when facing more complex cellular imageries. With more systems and investigations, we envision a similar machine learning method shall become a generic image analysis tool to benefit cellular-based bioscience and biomedical research.

Supplementary Material

Refer to Web version on PubMed Central for supplementary material.

References

1. Kroemer G, Galluzzi L, Vandenabeele P, Abrams J, Alnemri ES, Baehrecke EH, et al. Classification of cell death: recommendations of the Nomenclature Committee on Cell Death 2009. Cell Death and Differentiation. Jan.2009 16:3–11. [PubMed: 18846107]
2. Chen CS, Mrksich M, Huang S, Whitesides GM, Ingber DE. Geometric control of cell life and death. Science. May.1997 276:1425–1428. [PubMed: 9162012]
3. Elmore S. Apoptosis: A review of programmed cell death. Toxicologic Pathology. 2007; 35:495–516. [PubMed: 17562483]

4. Geiger B, Spatz JP, Bershadsky AD. Environmental sensing through focal adhesions. Nature Reviews Molecular Cell Biology. Jan.2009 10:21–33. [PubMed: 19197329]
5. Kaibuchi K, Kuroda S, Amano M. Regulation of the cytoskeleton and cell adhesion by the Rho family GTPases in mammalian cells. Annual Review of Biochemistry. 1999; 68:459–486.
6. Miettinen M, Lasota J. Gastrointestinal stromal tumors - Review on morphology, molecular pathology, prognosis, and differential diagnosis. Archives of Pathology & Laboratory Medicine. Oct.2006 130:1466–1478. [PubMed: 17090188]
7. Mizejewski GJ. Role of integrins in cancer: Survey of expression patterns. Proceedings of the Society for Experimental Biology and Medicine. Nov.1999 222:124–138. [PubMed: 10564536]
8. Potter JD. Morphogens, morphostats, microarchitecture and malignancy. Nature Reviews Cancer. Jun.2007 7:464–474. [PubMed: 17522715]
9. Sharma S, Sharma MC, Sarkar C. Morphology of angiogenesis in human cancer: a conceptual overview, histoprognostic perspective and significance of neoangiogenesis. Histopathology. May. 2005 46:481–489. [PubMed: 15842629]
10. Yeung T, Georges PC, Flanagan LA, Marg B, Ortiz M, Funaki M, et al. Effects of substrate stiffness on cell morphology, cytoskeletal structure, and adhesion. Cell Motility and the Cytoskeleton. Jan.2005 60:24–34. [PubMed: 15573414]
11. Shaked NT, Satterwhite LL, Telen MJ, Truskey GA, Wax A. Quantitative microscopy and nanoscopy of sickle red blood cells performed by wide field digital interferometry. Journal of Biomedical Optics. Mar.2011 16
12. Stuart MJ, Nagel RL. Sickle-cell disease. Lancet. Oct.2004 364:1343–1360. [PubMed: 15474138]
13. Banchereau J, Briere F, Caux C, Davoust J, Lebecque S, Liu YT, et al. Immunobiology of dendritic cells. Annual Review of Immunology. 2000; 18:767–811.
14. Banchereau J, Steinman RM. Dendritic cells and the control of immunity. Nature. Mar.1998 392:245–252. [PubMed: 9521319]
15. Xing F, Wang J, Hu M, Yu Y, Chen G, Liu J. Comparison of immature and mature bone marrow-derived dendritic cells by atomic force microscopy. Nanoscale Research Letters. Jul 16.2011 6
16. Lutz MB, Kukutsch N, Ogilvie ALJ, Rossner S, Koch F, Romani N, et al. An advanced culture method for generating large quantities of highly pure dendritic cells from mouse bone marrow. Journal of Immunological Methods. Feb 1.1999 223:77–92. [PubMed: 10037236]
17. Echlin P. The Application of Scanning Electron Microscopy to Biological Research. Philosophical Transactions of the Royal Society of London. B, Biological Sciences. 1971; 261:51–59.
18. Engel A, Colliex C. Application of scanning transmission electron microscopy to the study of biological structure. Current Opinion in Biotechnology. 1993 Aug 1.4:403–411. [PubMed: 7763970]
19. Carr KE, Toner PG. Scanning electron microscopy in biomedical research and routine pathology. Journal of Microscopy. 1981; 123:147–159. [PubMed: 7328636]
20. Kirk S, Skepper J, Donald AM. Application of environmental scanning electron microscopy to determine biological surface structure. Journal of Microscopy-Oxford. Feb.2009 233:205–224.
21. McCully ME, Canny MJ, Huang CX. Cryo-scanning electron microscopy (CSEM) in the advancement of functional plant biology. Morphological and anatomical applications. Functional Plant Biology. 2009; 36:97–124.
22. Okada T, Ogura T. Nanoscale imaging of untreated mammalian cells in a medium with low radiation damage using scanning electron-assisted dielectric microscopy. Scientific Reports. Jul. 2016 6
23. Ushiki T, Hitomi J, Ogura S, Umemoto T, Shigeno M. Atomic force microscopy in histology and cytology. Archives of Histology and Cytology. Dec.1996 59:421–431. [PubMed: 9037379]
24. Hoh JH, Hansma PK. Atomic force microscopy for high-resolution imaging in cell biology. Trends in Cell Biology. 1992 Jul 1.2:208–213. [PubMed: 14731502]
25. Lal R, John SA. BIOLOGICAL APPLICATIONS OF ATOMIC-FORCE MICROSCOPY. American Journal of Physiology. Jan.1994 266:C1-&. [PubMed: 8304408]
26. Francis LW, Lewis PD, Wright CJ, Conlan RS. Atomic force microscopy comes of age. Biology of the Cell. Feb.2010 102:133–143.

27. Firtel M, Beveridge TJ. Scanning probe microscopy in microbiology. Micron. 1995; 26:347–362. [PubMed: 8574524]
28. Deng Z, Lulevich V, Liu F-t, Liu G-y. Applications of Atomic Force Microscopy in Biophysical Chemistry of Cells. Journal of Physical Chemistry B. May 13.2010 114:5971–5982.
29. Deng Z, Weng IC, Li J-R, Chen H-Y, Liu F-T, Liu G-Y. Engineered Nanostructures of Antigen Provide an Effective Means for Regulating Mast Cell Activation. Acs Nano. Nov.2011 5:8672–8683. [PubMed: 21999491]
30. Deng Z, Zink T, Chen H-y, Walters D, Liu F-t, Liu G-y. Impact of Actin Rearrangement and Degranulation on the Membrane Structure of Primary Mast Cells: A Combined Atomic Force and Laser Scanning Confocal Microscopy Investigation. Biophysical Journal. Feb 18.2009 96:1629–1639. [PubMed: 19217878]
31. Shi LK, Zhao A, Salmeron J, Liu MGY. High-Resolution Imaging of Cells Using Current Sensing Atomic Force Microscopy. Letters in Applied NanoBioScience. 2015; 4:316–320.
32. Rangamani P, Levy MG, Khan S, Oster G. Paradoxical signaling regulates structural plasticity in dendritic spines. Proceedings of the National Academy of Sciences. Sep 6.2016 113:E5298–E5307.
33. Rangamani P, Lipshtat A, Azeloglu Evren U, Calizo Rhodora C, Hu M, Ghassemi S, et al. Decoding Information in Cell Shape. Cell. Sep 12.2013 154:1356–1369. [PubMed: 24034255]
34. Neves SR, Tsokas P, Sarkar A, Grace EA, Rangamani P, Taubenfeld SM, et al. Cell Shape and Negative Links in Regulatory Motifs Together Control Spatial Information Flow in Signaling Networks. Cell. May 16.2008 133:666–680. [PubMed: 18485874]
35. Xiong Y, Rangamani P, Fardin M-A, Lipshtat A, Dubin-Thaler B, Rossier O, et al. Mechanisms Controlling Cell Size and Shape during Isotropic Cell Spreading. Biophysical Journal. May 19.2010 98:2136–2146. [PubMed: 20483321]
36. Rangamani P, Agrawal A, Mandadapu KK, Oster G, Steigmann DJ. Interaction between surface shape and intra-surface viscous flow on lipid membranes. Biomechanics and Modeling in Mechanobiology. 2013; 12:833–845. [PubMed: 23086137]
37. Rangamani P, Fardin M-A, Xiong Y, Lipshtat A, Rossier O, Sheetz MP, et al. Signaling Network Triggers and Membrane Physical Properties Control the Actin Cytoskeleton-Driven Isotropic Phase of Cell Spreading. Biophysical Journal. Feb 16.2011 100:845–857. [PubMed: 21320428]
38. Torres AJ, Wu M, Holowka D, Baird B. Nanobiotechnology and Cell Biology: Micro- and Nanofabricated Surfaces to Investigate Receptor-Mediated Signaling. Annu Rev Biophys. 2008; 37:265–288. [PubMed: 18573082]
39. Altomare L, Fare S. Cells response to topographic and chemical micropatterns. Journal of Applied Biomaterials & Biomechanics. Oct-Dec;2008 6:132–143. [PubMed: 20740457]
40. Qian TC, Wang YX. Micro/nano-fabrication technologies for cell biology. Medical & Biological Engineering & Computing. Oct.2010 48:1023–1032. [PubMed: 20490938]
41. Bettinger CJ, Langer R, Borenstein JT. Engineering substrate topography at the micro- and nanoscale to control cell function. Angewandte Chemie-International Edition. 2009; 48:5406–5415. [PubMed: 19492373]
42. Manz BN, Groves JT. Spatial organization and signal transduction at intercellular junctions. Nature Reviews Molecular Cell Biology. May.2010 11:342–352. [PubMed: 20354536]
43. Li J-R, Ross SS, Liu Y, Liu YX, Wang K-h, Chen H-Y, et al. Engineered Nanostructures of Haptens Lead to Unexpected Formation of Membrane Nanotubes Connecting Rat Basophilic Leukemia Cells. Acs Nano. Jul.2015 9:6738–6746. [PubMed: 26057701]
44. Li J-R, Shi L, Deng Z, Lo SH, Liu G-y. Nanostructures of Designed Geometry and Functionality Enable Regulation of Cellular Signaling Processes. Biochemistry. Jul 31.2012 51:5876–5893. [PubMed: 22783801]
45. Bakal C, Aach J, Church G, Perrimon N. Quantitative morphological signatures define local signaling networks regulating cell morphology. Science. Jun.2007 316:1753–1756. [PubMed: 17588932]
46. Metcalfe DD, Baram D, Mekori YA. Mast cells. Physiological Reviews. Oct.1997 77:1033–1079. [PubMed: 9354811]

47. Pfeiffer JR, Seagrave JC, Davis BH, Deanin GG, Oliver JM. Membrane and Cytoskeletal Changes Associated with IgE-Mediated Serotonin Release from Rat Basophilic Leukemia Cells. J Cell Biol. 1985; 101:2145–2155. [PubMed: 2933414]
48. Holowka D, Sil D, Torigoe C, Baird B. Insights into Immunoglobulin E Receptor Signaling from Structurally Defined Ligands. Immunol Rev. Jun.2007 217:269–279. [PubMed: 17498065]
49. Torres AJ, Vasudevan L, Holowka D, Baird BA. Focal Adhesion Proteins Connect IgE Receptors to the Cytoskeleton as Revealed by Micropatterned Ligand Arrays. P Natl Acad Sci U S A. Nov 11.2008 105:17238–17244.
50. Jones TR, Carpenter AE, Lamprecht MR, Moffat J, Silver SJ, Grenier JK, et al. Scoring diverse cellular morphologies in image-based screens with iterative feedback and machine learning. Proceedings of the National Academy of Sciences of the United States of America. Feb.2009 106:1826–1831. [PubMed: 19188593]
51. Loo L-H, Wu LF, Altschuler SJ. Image-based multivariate profiling of drug responses from single cells. Nature Methods. May.2007 4:445–453. [PubMed: 17401369]
52. Gross B, Hanna D. 3D Virtual Videos of Brain Chemistry Using Spatiotemporal Neural Networks. Journal of Pattern Recognition. 2010; 43:3910–3921.
53. Haskell RE, Li P, Hanna D. Using a Genetic Algorithm to Optimize the Performance of Classification Tree Fuzzy Systems. Journal of Pattern Recognition. 2004; 37:1653–1659.
54. Haskell, RE., Hanna, D., Li, P., Cheok, KC., Hudas, G. Finding Pattern Behavior in Temporal Data using Fuzzy Clustering. Procedings of the Conference on Artificial Neural Networks in Engineering; St. Louis. 2000.
55. Serra, J. Image Analysis and Mathematical Morphology. Academic Press; 1982.
56. Otsu N. A Threshold Selection Method from Gray-Level Histograms. IEEE Transactions on Systems, Man, and Cybernetics. 1979; 9:62–66.
57. Ojala T, Pietikainen M, Maenpaa T. Multiresolution gray-scale and rotation invariant texture classification with local binary patterns. Ieee Transactions on Pattern Analysis and Machine Intelligence. Jul.2002 24:971–987.
58. Dalal, N., Triggs, B. Histograms of oriented gradients for human detection. In: Schmid, C.Soatto, S., Tomasi, C., editors. 2005 IEEE Computer Society Conference on Computer Vision and Pattern Recognition, Vol 1, Proceedings. 2005. p. 886-893.
59. Zhu, Q., Yeh, M-C., Cheng, K-T., Avidan, S. Fast Human Detection Using a Cascade of Histograms of Oriented Gradients. presented at the Proceedings of the 2006 IEEE Computer Society Conference on Computer Vision and Pattern Recognition - Volume 2; 2006.
60. Suard F, Rakotomamonjy A, Bensrhair A, Broggi A. Ieee. Pedestrian detection using infrared images and histograms of oriented gradients. 2006
61. Gonzalez, RC., Woods, RE. Digital Image Processing. 3. Pearson Education, Inc; 2008.
62. Zhou N, Wang L. A modified T-test feature selection method and its application on the HapMap genotype data. Genomics, proteomics & bioinformatics. 2007; 5:242–249.
63. Chu F, Wang L. Applications of support vector machines to cancer classification with microarray data. International journal of neural systems. 2005; 15:475–484. [PubMed: 16385636]
64. Salas-Gonzalez D, Górriz JM, Ramírez J, López M, Alvarez I, Segovia F, et al. Computer-aided diagnosis of Alzheimer's disease using support vector machines and classification trees. Physics in Medicine and Biology. 2010; 55:2807. [PubMed: 20413829]
65. Fan R-E, Chen P-H, Lin C-J. Working set selection using second order information for training support vector machines. Journal of machine learning research. 2005; 6:1889–1918.
66. Chapelle O, Haffner P, Vapnik VN. Support vector machines for histogram-based image classification. IEEE transactions on Neural Networks. 1999; 10:1055–1064. [PubMed: 18252608]
67. Breiman, L., Friedman, J., Stone, CJ., Olshen, RA. Classification and Regression Trees. CRC press; 1984.
68. Conrad C, Erfle H, Warnat P, Daigle N, Lorch T, Ellenberg J, et al. Automatic identification of subcellular phenotypes on human cell arrays. Genome Research. Jun.2004 14:1130–1136. [PubMed: 15173118]

69. Masood, A., Al-Jumaily, A. Differential evolution based advised SVM for histopathalogical image analysis for skin cancer detection. 2015 37th Annual International Conference of the IEEE Engineering in Medicine and Biology Society (EMBC); 2015. p. 781-784.

70. Beleites C, Baumgartner R, Bowman C, Somorjai R, Steiner G, Salzer R, et al. Variance Reduction in Estimating Classification Error using Sparse Datasets. Chemometrics and intelligent laboratory systems. 2005; 79:91–100.

71. Rotsch C, Radmacher M. Drug-induced changes of cytoskeletal structure and mechanics in fibroblasts: An atomic force microscopy study. Biophysical Journal. Jan.2000 78:520–535. [PubMed: 10620315]

72. Touhami A, Nysten B, Dufrene YF. Nanoscale mapping of the elasticity of microbial cells by atomic force microscopy. Langmuir. May.2003 19:4539–4543.

73. Matzke R, Jacobson K, Radmacher M. Direct, high-resolution measurement of furrow stiffening during division of adherent cells. Nature Cell Biology. Jun.2001 3:607–610. [PubMed: 11389447]

74. Seiler H. SECONDARY-ELECTRON EMISSION IN THE SCANNING ELECTRON-MICROSCOPE. Journal of Applied Physics. 1983; 54:R1–R18.

75. Bogner A, Jouneau PH, Thollet G, Basset D, Gauthier C. A history of scanning electron microscopy developments: Towards “wet-STEM” imaging. Micron. 2007; 38:390–401. [PubMed: 16990007]

76. Stokes DJ. Recent advances in electron imaging, image interpretation and applications: environmental scanning electron microscopy. Philosophical Transactions of the Royal Society of London Series a-Mathematical Physical and Engineering Sciences. Dec.2003 361:2771–2787.

77. Valim CXR, da Silva EZM, Assis MA, Fernandes FF, Coelho PSR, Oliver C, et al. rPbPga1 from Paracoccidioides brasiliensis Activates Mast Cells and Macrophages via NFkB. PLoS Neglected Tropical Diseases. 2015; 9:e0004032. [PubMed: 26317855]

Biographies

Michael F. Lohrer received his B.S. in computer engineering from Oakland University, Rochester, Michigan in 2013 and M.S. degree in embedded systems also from Oakland University in 2015. He is currently pursuing the Ph.D. degree in electrical and computer engineering at Oakland University. Since 2013 he has been a Research Assistant with the Nanoimaging Laboratory at Oakland University. From 2014 to 2015 he worked as an Engineer at RHK Technology, Inc, and during the summers of 2015 and 2016 he worked as a Software Engineer at Dataspeed, Inc. His research interests include artificial intelligence, high-speed embedded systems, nanoimaging, and robotics.

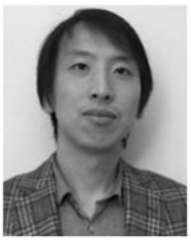

Yang Liu is a graduate student in the Department of Chemistry, University of California, Davis. He received his bachelor of science degree at Peking University, China in 2011. Currently, he is pursuing a Ph.D. degree in chemistry under G. Liu's supervision. His research focuses on interactions between cells and 2D nanopattern of designed ligands. He has 5 publications, as of today, and is a recipient of UCD-LLNL Graduate Fellowship.

Darrin M. Hanna (M'99) received his B.S. in computer engineering and mathematics and M.S. degree in computer science and engineering from Oakland University, Rochester, Michigan, in 1999 and Ph.D. in systems engineering from Oakland University in 2003. From 2003–2009, he was Assistant Professor of Engineering in the Department of Electrical and Computer Engineering and from 2009–2017 he was Associate Professor of Engineering and since 2017 Professor of Engineering in the Department of Electrical and Computer Engineering and Director of the Nanoimaging Laboratory at Oakland University. Since 1999 he has served as Consultant to several companies for research, development, and commercialization. He is the author of 14 books, more than 50 articles, and 3 licensed technologies. His research interested include artificial intelligence, high-speed embedded systems, and nanoimaging. Professor Hanna is a Member of IEEE and ASEE. He was the recipient of the 2007 IEEE Computer Society Computer Science and Engineering Undergraduate Teaching Award.

Gang-yu Liu received her Ph.D. in chemistry in 1992 from Princeton University, NJ. After 2 years of postdoctoral research as a Miller Research Fellow at UC Berkeley, she became an assistant professor at Wayne State University in 1994. In 2001, she moved to University of

California, Davis, CA, where she became professor of chemistry in 2005. Her research focuses on methodology development of 2D and 3D nanolithography, high-resolution material and bioimaging, and using nanotechnology to investigate and control cellular signaling processes. She also directs the Keck Spectral Imaging Facility (KSIF), a campus core facility at UC Davis. She has over 100 publications, and numerous book chapters and US Patents. Professor Liu is a Member of AAAS, ACS, ACBS, APS and BPS. She has received numerous awards for her research in nanotechnology and nanobiotechnology, including Beckman Young Investigator Award, Fellow of ACS and Fellow of AAAS.

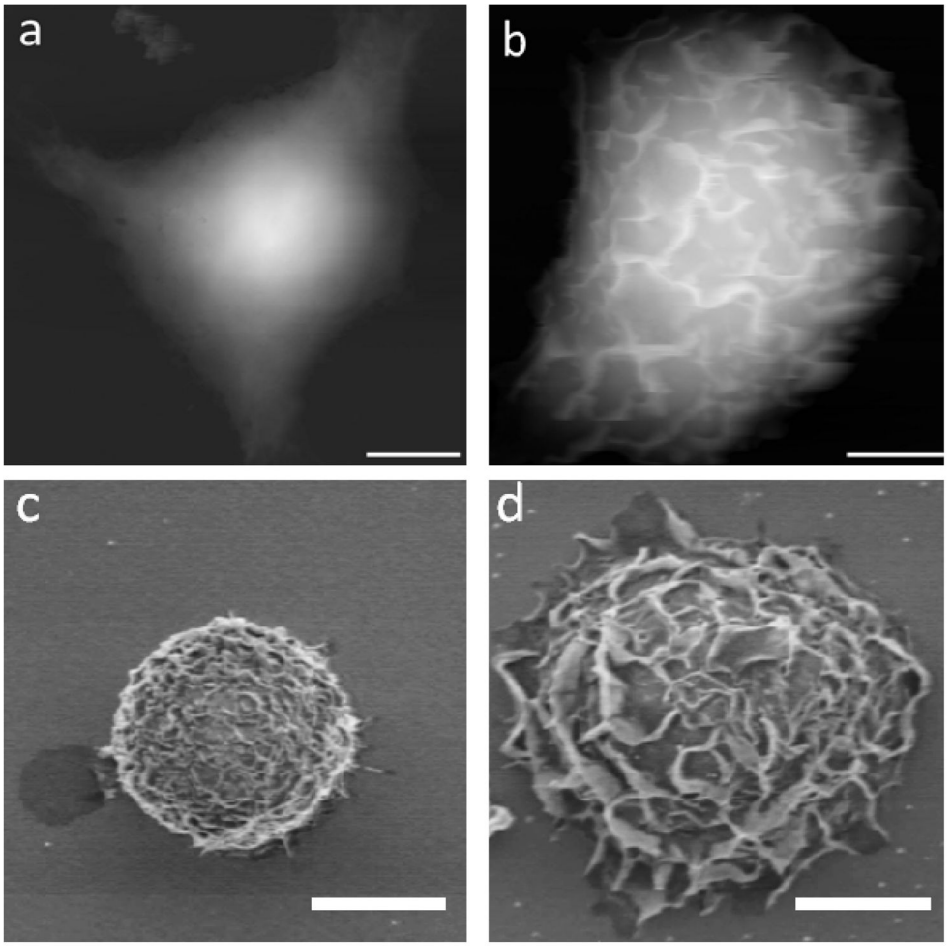

Fig. 1.

Characteristic AFM images of (a) a resting RBL cell, and (b) an activated RBL cell. Characteristic SEM images of (c) a resting RBL cell, and (d) an activated RBL cell. Scale bar equals 5 μm.

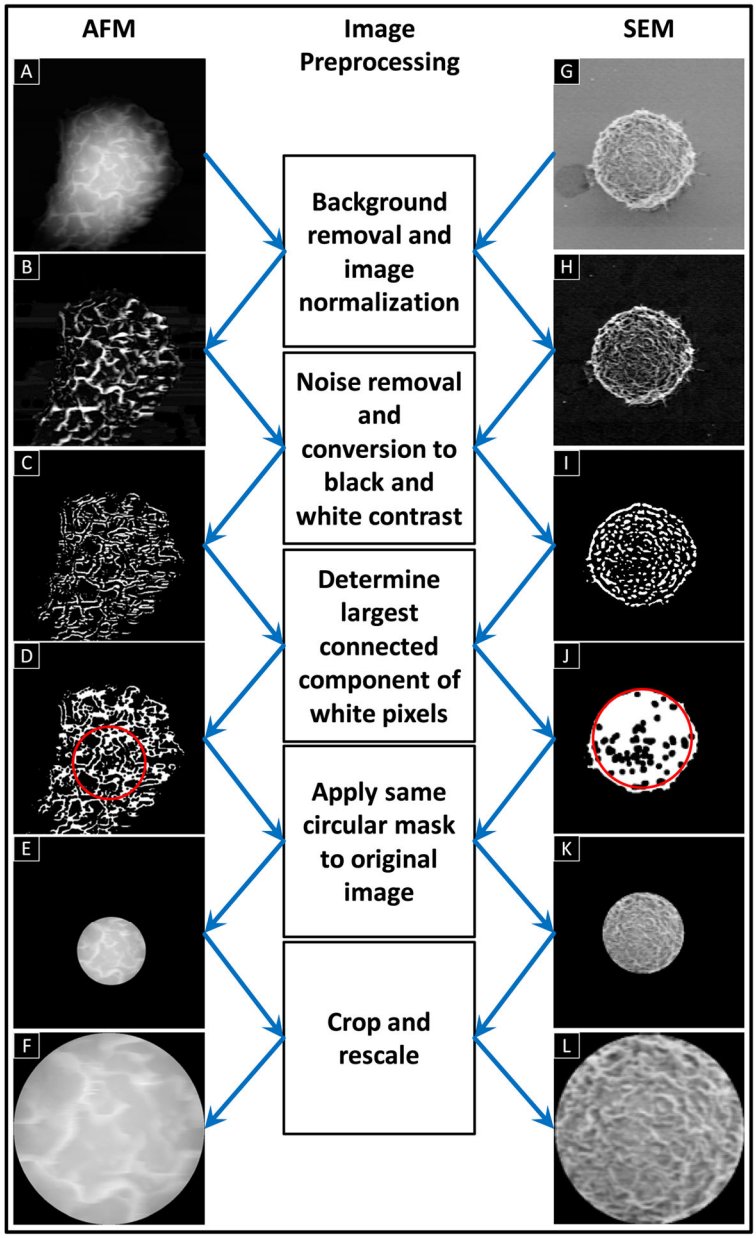

Fig. 2.

Key steps in our data processing (middle) and the outcome in each step using an example AFM image (left) and an SEM image (right).

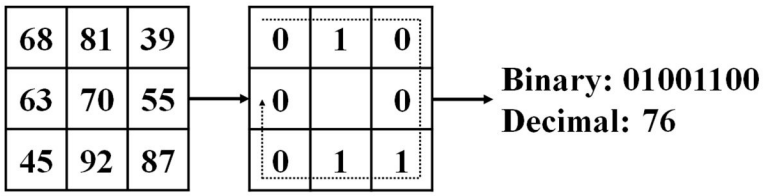

Fig. 3.
An example illustrating LBP: a section of grayscale image to binary code.

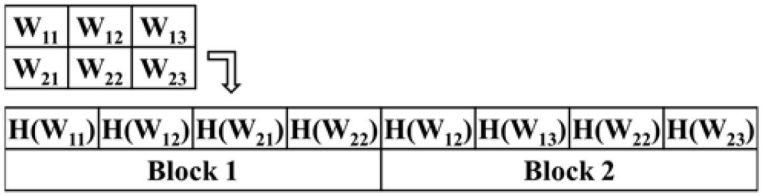

Fig. 4.
Example section of grayscale image to binary code blocks.

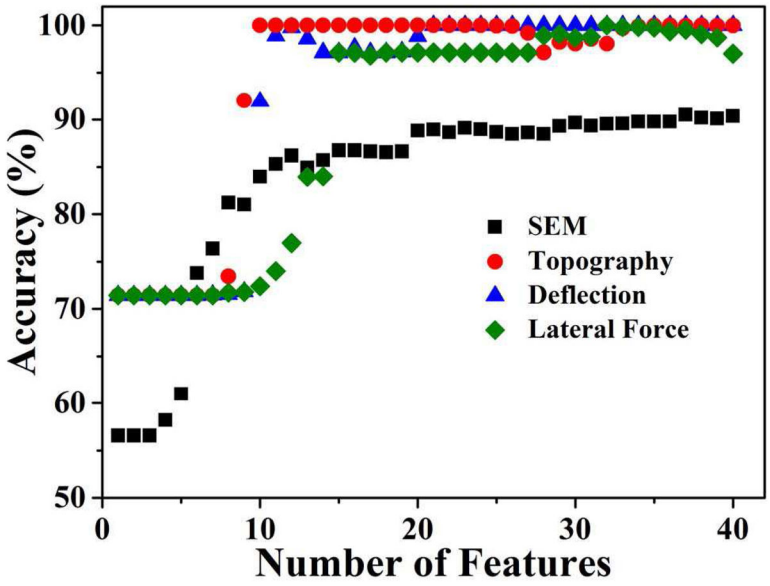

Fig. 5.

Accuracy of activation classification from AFM images as a function of the number of features used. AFM image types include topography, deflection and lateral force contrast, respectively. Results from SEM images are also included for comparison. In each data point, the standard deviation was within ± 3%.

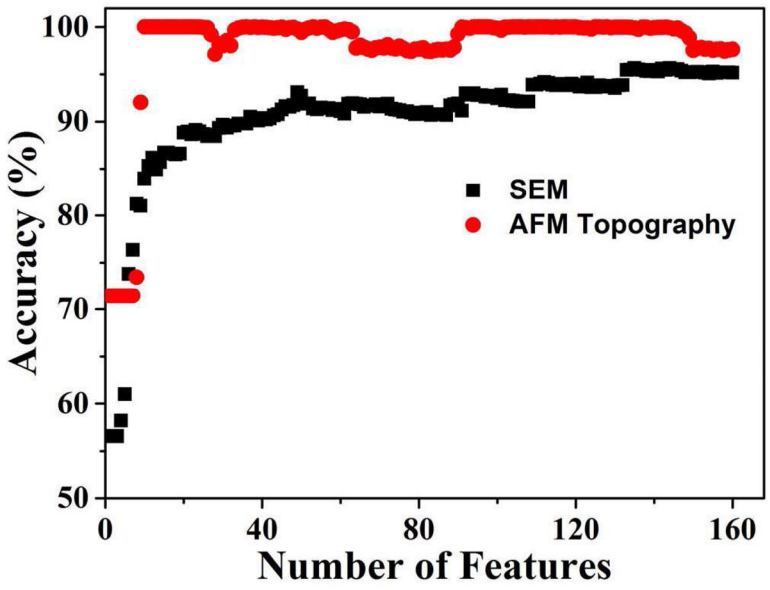

Fig. 6.

Accuracy of both SEM and AFM classification versus the number of features used. For all experiments with greater than 10 features, the standard deviation was within ±1.5%. Experiments with between 1 and 10 features had standard deviation within ±3%.

Author Manuscript

Author Manuscript

Author Manuscript

TABLE I

Classification Results From AFM Topography Images

	40 Features		135 Features	
	True Resting	**True Activated**	**True Resting**	**True Activated**
Predicted Resting	10 ± 0	0 ± 0	10 ± 0	0 ± 0
Predicted Activated	0 ± 0	25 ± 0	0 ± 0	25 ± 0
Average Accuracy (%)	100		100	

TABLE II

Classification Results From SEM Images

	40 Features		135 Features	
	True Resting	**True Activated**	**True Resting**	**True Activated**
Predicted Resting	38.9 ± 0.9	5.7 ± 0.5	41 ± 0	2.6 ± 0.6
Predicted Activated	4.1 ± 0.9	50.3 ± 0.5	2 ± 0	53.4 ± 0.6
Average Accuracy (%)	90.1		95.4	